International Journal of Geo-Information

MDPI

Article

Study on LOS to Vertical Deformation Conversion Model on Embankment Slopes Using Multi-Satellite SAR Interferometry

Jie Liu, Tao Li *, Sijie Ma, Qiang Shan and Weiping Jiang

Global Navigation Satellite System (GNSS) Research Centre, Wuhan University, Wuhan 430079, China; liujie-insar@whu.edu.cn (J.L.); 2020206180033@whu.edu.cn (S.M.); qiangshan@whu.edu.cn (Q.S.); wpjiang@whu.edu.cn (W.J.)

* Correspondence: taoli@whu.edu.cn; Tel.: +86-27-6877-8005; Fax: +86-27-6877-8971

Abstract: Slant range geometry plays a crucial role in interpreting synthetic aperture radar (SAR) observations, especially in converting line-of-sight (LOS) surface deformations to actual vertical subsidence. This paper proposes a new conversion model to retrieve vertical settlements of the embankment slopes using the geometrical parameters of the dam and the SAR sensor. The simulation results highlight the impact of slope foreshortening and heading direction of the satellite on deformation retrieval. Various SAR data with different resolutions and bands are used to analyze the model's performance, revealing a high conformity of the model with practical conversion parameters exceeding 80% for TerraSAR-X and Cosmo-SkyMed data.

Keywords: multi-satellite; InSAR; deformation; dam; scale effect

Citation: Liu, J.; Li, T.; Ma, S.; Shan, Q.; Jiang, W. Study on LOS to Vertical Deformation Conversion Model on Embankment Slopes Using Multi-Satellite SAR Interferometry. *ISPRS Int. J. Geo-Inf.* **2024**, *13*, 58. https://doi.org/10.3390/ijgi13020058

Academic Editors: Diego González-Aguilera, Pablo Rodríguez-González and Wolfgang Kainz

Received: 28 October 2023
Revised: 30 January 2024
Accepted: 6 February 2024
Published: 14 February 2024

1. Introduction

In China, there are nearly 100,000 earth and rock-filled dams serving as critical infrastructures for irrigation, food security, flood control, and power generation [1]. The routine monitoring of surface deformation in the dam is crucial for safety assessments [2–4]. There are three forces that can affect dam deformation. These are (1) the load of the dam, (2) the inner consolidation of the dam earth, and (3) the water pressure from the reservoir [5–7]. The post-construction settlement, caused by inner earth consolidation, is an important index for dam security that is often monitored by the total station and GNSS. Due to its high accuracy (mm-cm) and spatial resolution (0.5–10 m), interferometric synthetic aperture radar (InSAR) has become a preferred geodetic method for deformation monitoring related to large-scale infrastructures, such as dams, long bridges, and so on [8–10]. The escalating investment in clean energy has led to the construction of a lot of hydropower and pumped storage, including small and middle-sized earth and rock-filled dams. High-resolution InSAR provides accurate and detailed insights about dam surface deformation, allowing for early detection of potential issues related to post-construction settlement and other forces influencing dam stability.

Numerous research articles present findings from the utilization of moderate-resolution InSAR products for monitoring surface deformation in large dams. In 2012, Wang et al. [6] employed the permanent scatterer-InSAR (PS-InSAR) method with Envisat data to analyze the stability of the Three Gorges Dam after the full reservoir impoundment. The PS points on the dam showed that the deformation curves were consistent with the water pressure during the impoundment process. Neokosmidis et al. [3] used ERS and Envisat data to monitor Mornos Dam deformation and detected the effect of five strong seismic events with epicenters close to the dam. The PS-InSAR results by the ENVISAT dataset from Grenerczy et al. [11] showed that the collapse of the red earth dam in Hungary started at the position with the maximum deformation. Di Martire et al. [12] used Envisat data to monitor the post-construction settlement of the Conza Dam in Italy and found that the InSAR results are consistent with the leveling measurements and the inner pressure

sensors. Using the L-band ALOS-1 SAR image, Zhou et al. measured more than 40 cm of post-construction settlement on the Shuibuya Dam surface [13]. These results were valuable for using the finite element model in evaluating the safety of the Shuibuya Dam with a height of 230 m [14]. Utilizing Sentinel1-based PS-InSAR results, Al-Husseinawi et al. found that the Darbandikhan Dam crest area sustained continuous deformation between November 2017 and March 2018 [7]. S. L. Ullo et al. evaluated the stability of the Campolattaro Dam in Italy based on DInSAR results and detected a millimeter-level settlement of the Campolattaro Dam in around seven months in 2016 [15]. However, in all the above cases, it is difficult to determine the precise position of PS points and convert the LOS deformation derived from SAR geometry into dam settlement geometry due to the moderate resolution of SAR images and the lack of high precision DEM of the dam.

Through high-resolution X-band SAR images provided by TerraSAR Spotlight data, the differential interferometric fringes on the surface of the dam can be clearly extracted much better than moderate and lower resolution C-band and L-band SAR images [5,13]. Research by [5] indicates that even SAR images with a 1-m resolution face challenges in accurately capturing deformation information when the dam crest's deformation gradient is excessively large. Taking into account the compression factor of dam planes, Al-Husseinawi et al. [7] presented the maximum detectable gradient of deformation, revealing the difficulty in monitoring dam deformation induced by a nearby earthquake using Sentinel-1 data. Li et al. [16] analyzed the difference between COSMOS and TerraSAR-X data in terms of deformation assessment of the earth-rock dams in Gongming Reservoir. The actual measurement results show that the low-resolution data reduce the reliability of the deformation results of PS points [16]. The above literature is concerned with exemplary studies on the scale effect of multi-resolution SAR images for dam slope deformation monitoring. However, a systematic theoretical study and quantitative analysis on this topic are still lacking.

According to the side-looking geometry, we can directly measure the line of sight (LOS) displacement of the embankment slope in InSAR results. In order to decompose InSAR LOS motion (1D) into a 3D deformation, parameters such as high-resolution DEM, slope angle, a priori model of the surface motion, and so forth, are needed to perform point-by-point conversion [17]. When both ascending and descending SAR data are available, the horizontal (mainly east-west direction) and vertical deformation can be derived. Many works have presented the successful applications of such decomposition for various applications [11,18,19]. Alessandro et al. [19] acquired the vertical and horizontal ground velocities of the Etna volcano flanks by combining the ascending and descending ERS data and proposed a new kinematic model of the Etna volcano. Eriksen et al. [19] studied several landslide areas in Norway by PS technology using ascending and descending data, and the acquired 2D deformation of landslide slopes helped the division of landslide sub-blocks and the analysis of movement mechanism [19]. Li et al. analyzed the LOS deformation difference due to the various local incident angles from different parts of the dam slope and proposed a LOS to vertical deformation correction model to correct the time series deformation of the Gongming Reservoir in Shenzhen, China [16].

In this paper, we assess measurement capability from currently operating X-band and C-band SAR sensors for evaluating post-construction settlements of the small and middle-sized earth-filled dams. Within the theoretical background in section II, we propose a conversion factor to retrieve vertical settlements of the embankment slopes based on the geometrical parameters of the dam and acquisition parameters of SAR sensors. To show the impact and necessity of deformation conversion, the simulation experiment with different dam cross angles under multi-satellite SAR data is first conducted. Finally, we apply the proposed methodology to evaluate post-construction settlements of the Gongming embankment dams in Shenzhen City in China using various SAR sensors including TerraSAR-X in spotlight mode, CSK data in stripmap mode, and Sentinel-1 data in TOPS mode.

2. SAR Side-Looking Geometry and Compression Factors Due to Foreshortening

2.1. The SAR Distortion Geometry on Dam Cross Section

Figure 1 depicts a cross-section of an embankment dam, where the fore-slope angle is denoted as α and the back-slope angle is denoted as β. In this scenario, we assume that the dam axis is parallel to the SAR heading, and the local incident angle is η_c. Based on the slope angles of α and β, the local incidence angle on the fore-slope and back-slope changes to η_α and η_b, respectively. These angles can be calculated using the following equations:

$$\begin{aligned} \eta_a &= \eta_c - \alpha \\ \eta_b &= \eta_c + \beta \end{aligned} \tag{1}$$

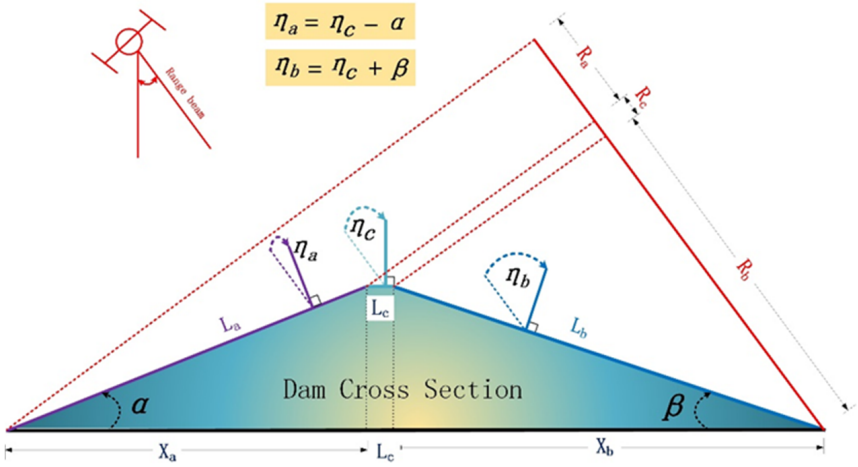

Figure 1. The local incidence angle changes on the dam surface (Dam cross-section in radar reflection geometry).

Based on the SAR side-looking geometry depicted in Figure 1, the length L_a of the fore-slope in the dam cross-section corresponds to the ground range of X_a, L_b on the back-slope corresponds to the ground range of X_b, and L_c is the crest cross-section length. When the cross-section lengths of those slopes are projected in SAR range geometry, they correspond to R_a,R_b, and R_c, respectively. The following equations can be used to calculate the foreshortening of dam slopes cross-section lines in SAR geometry:

$$\begin{aligned} R_a &= L_a \times \sin(\eta_a) \\ R_b &= L_b \times \sin(\eta_b) \\ R_c &= L_c \times \sin(\eta_c) \end{aligned} \tag{2}$$

In Figure 1, the fore-slope, directly facing the radar beam, exhibits a smaller local incidence angle η_a and results in a shorter radar-range projection R_a. On the contrary, the back slope features a larger local incidence angle η_b, leading to a longer radar-range projection R_b. It is essential to note that Figure 1 illustrates a very specific condition of the dam slope cross section that is perpendicular to the SAR heading direction. In general, the dams' axis may not be parallel to the SAR heading direction, necessitating modifications to Equation (2).

This modification has been illustrated visually in Figure 2, where Figure 2a presents a 3D perspective of an embankment, while Figure 2b depicts a 2D diagram for the dam perspective view in SAR side-looking geometry. The symbol ϕ in Figure 2 represents the rotation angle between the dam axis and the SAR heading direction.

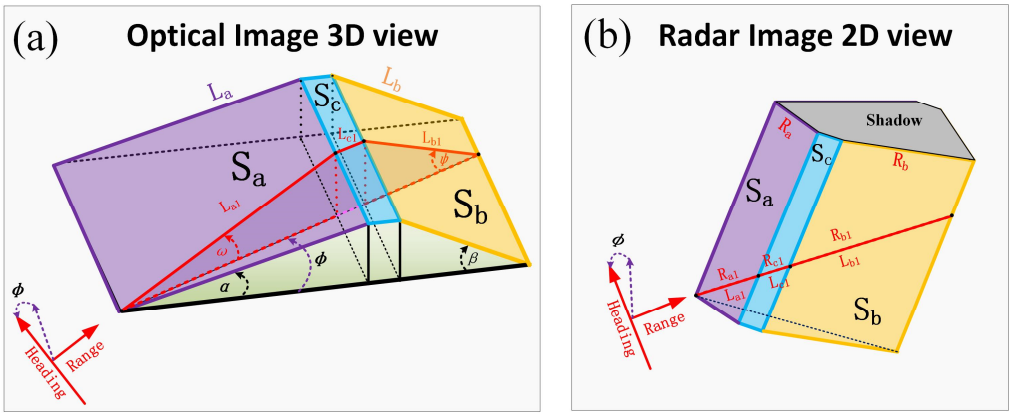

Figure 2. An angle ϕ between the dam axis and the SAR heading direction (**a**) Dam's 3D Optical perspective. (**b**) Dam's 2D perspective view in SAR geometry.

In Figure 2a, the symbols of ω and ψ represent slope angles in the LOS cross-section. The local incidence angle on S_a is changed to η_{a1}, and the local incidence angle on S_b is changed to η_{b1}. These parameters can be calculated through the following equations:

$$\begin{aligned} \omega &= tan^{-1}(tan(\alpha) \times cos\phi) \\ \psi &= tan^{-1}(tan(\beta) \times cos\phi) \\ \eta_{a1} &= \eta_c - \omega \\ \eta_{b1} &= \eta_c + \psi \end{aligned} \tag{3}$$

When the dam axis is parallel to the SAR heading direction (i.e., $\phi = 0$), Equation (3) is equivalent to Equation (1). In the case where $\phi = 90$, we have $\eta_{a1} = \eta_{b1} = \eta_c$.

By combining (1, 2, and 3), we can simulate dam distortion in SAR geometry using the dam's design map and SAR acquisition parameters. On the other hand, the above equations prove valuable for selecting suitable SAR products with ideal local incidence angles for dam deformation monitoring.

2.2. Slope Deformation Conversion in Side-Looking Geometry

Theoretically, the vertical surface deformation on the earth's ground should be calculated from LOS measurements by a cosine formula corresponding to the SAR local incidence angle. However, this method is based on the assumption that the deformation only occurs in a vertical direction, without considering the earth-filled dam's post-construction deformation model. As discussed in the previous section, the local incidence angle varies according to the dam slope angle. As the dam only has three slopes with a trapezium cross-section to the range direction, the slope deformation on the dam can be modeled with specific equations.

Figure 3 shows a post-construction settlement in a dam cross-section, assuming the dam axis is parallel to the SAR heading direction. The dam post-construction settlement primarily results from the consolidation of the filled earth and rock, with the settlement rate proportionate to the earth-filling height during the rapid consolidation processing [16,20]. The longer black arrows on the dam's top indicate larger deformation on the crest while the shorter black arrows in the middle of the two slopes represent smaller deformation at those locations.

According to the post-construction settlement mechanism of earth and rock-filled dams, small and middle-sized dams settle due to the compaction effect of filling earth throughout the construction period and for 1~2 years after the post-construction period. In SAR geometry, only the line-of-sight projection of the slope surface deformation is visible along the radar beam. Assuming that for each dam slope there is a uniform normal deformation (deformation along local normal direction) denoted as Δd, the corresponding

LOS motion in SAR geometry is represented as ΔR_a, ΔR_b, and ΔR_c. These can be calculated using the following equations:

$$\begin{aligned} \Delta R_a &= \Delta d \cdot \cos \eta_a \\ \Delta R_b &= \Delta d \cdot \cos \eta_b \\ \Delta R_c &= \Delta d \cdot \cos \eta_c \end{aligned} \tag{4}$$

η_a, η_b, and η_c are the local incidence angles on the surface S_a, S_b, and S_c, respectively.

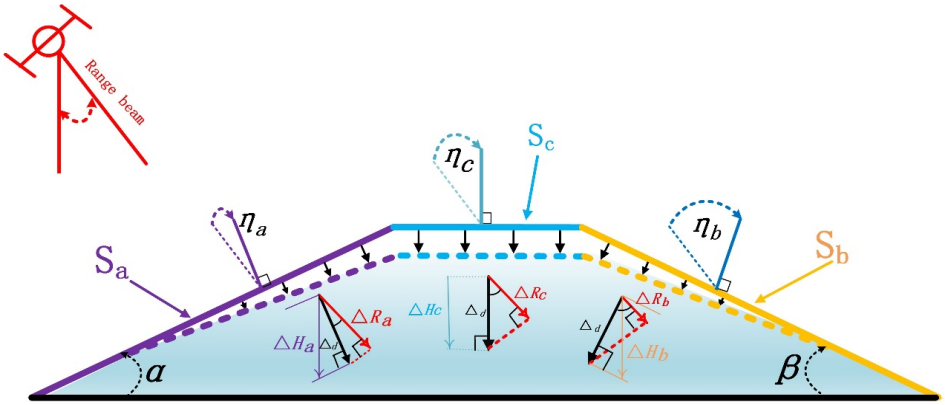

Figure 3. Dam post-construction settlement on cross-section in SAR geometry (Dam axis along SAR heading direction).

As illustrated in Figure 3, concerning the same normal deformation Δd on three surfaces, the slope S_a suffers the largest LOS deformation while the slope S_b suffers the smallest LOS. Considering the unique deformation characteristics of dam consolidation, we convert the deformation base on the entire slope, rather than a single point target. The nominal deformation Δd can be converted to vertical deformation by the following equations:

$$\begin{aligned} \Delta H_a &= \frac{\Delta d}{\cos \alpha} \\ \Delta H_b &= \frac{\Delta d}{\cos \beta} \\ \Delta H_c &= \Delta d \end{aligned} \tag{5}$$

ΔH_a, ΔH_b, and ΔH_c are vertical deformation for the three surfaces S_a, S_b, and S_c, respectively. As expected, ΔH_c is equivalent to Δd in terms of amount because the surface normal direction on the crest is parallel with the vertical direction. Combining Equations (4) and (5), we can derive the following equations concerning the relationship between the vertical deformation of the slopes and the SAR LOS deformation in each surface S_a, S_b, and S_c.

$$\begin{aligned} \Delta H_a &= \frac{\Delta R_a}{\cos \eta_a \cdot \cos \alpha} \\ \Delta H_b &= \frac{\Delta R_b}{\cos \eta_b \cdot \cos \beta} \\ \Delta H_c &= \frac{\Delta R_c}{\cos \eta_c} \end{aligned} \tag{6}$$

Regarding a general case, where the rotation angle ϕ exists between the dam axis and the SAR heading direction, (6) turns into:

$$\begin{aligned} \Delta H_{a1} &= \frac{\Delta R_{a1}}{\cos \eta_{a1} \cdot \cos \omega} \\ \Delta H_{b1} &= \frac{\Delta R_{b1}}{\cos \eta_{b1} \cdot \cos \psi} \\ \Delta H_c &= \frac{\Delta R_{c1}}{\cos \eta_c} \end{aligned} \tag{7}$$

ΔH_{a1}, ΔH_{b1}, and ΔH_{c1} are the vertical deformation on the surface S_a, S_b, and S_c. Similarly, ΔR_{a1}, ΔR_{b1}, andΔR_{c1} and η_{a1}, η_{b1}, and η_{c1} are the SAR LOS deformation and the local incidence angles on those surfaces, respectively.

By combining Equations (5)–(7), we can convert dam surface deformation to SAR LOS deformation, taking into account the dam's design map and SAR acquiring parameters, and vice versa. These equations will be instrumental in evaluating suitable SAR parameters for monitoring dam post-construction settlement.

According to Equations (6) and (7), we propose a universal conversion parameter ε for slope deformation conversion from SAR LOS direction to vertical in the side-looking geometry, which is calculated by the following equation:

$$\varepsilon = \cos\eta \cdot \cos\alpha \tag{8}$$

η is the slope local incidence angle, which is derived from the SAR LOS direction and the slope azimuth direction. α is the slope angle in the LOS direction measured from the horizontal surface. Therefore, the relation between LOS deformation and vertical settlement can be represented by the following equation:

$$\Delta R = \varepsilon \cdot \Delta H \tag{9}$$

Here, ΔR is the LOS deformation acquired by InSAR, ε is the conversion parameter, and ΔH is the vertical settlement of the slope. Once the slope is a horizontal surface ($\alpha = 0$), then we get $\varepsilon = \cos\eta$, which is the traditional equation for the SAR deformation conversion in flat areas. With respect to the special case where the dam axis is parallel to the SAR heading, α would be equal to the slope angle derived from topography. Therefore, Equation (9) could be applied in many conditions where there are similar uniform flat surfaces with small settlements, for instance, artificial embankment consolidation, landslide area small creeping processing, small expanding or shrinking volcanic surface, and so on.

3. Slope Settlement Simulation

To illustrate how the conversion parameter ε influences the deformation curves in SAR interferometry, this section employs the settlement of a small dam as an example for simulating DInSAR fringes with various SAR resolutions and with cross angles ϕ of 0°, 30°, 60°, and 90°.

In Figure 4a, the measurement unit in horizontal and vertical directions is millimeters. The simulated dam has a trapezoidal shape. The height of the trapezoid is 30 m, the top width of the trapezoid is 21 m, and the width and the length of the trapezoid are 185 and 265 m, with both the fore-slope and the back-slope angles being 20°. Figure 4b displays the front view of the dam, with the deformation trend indicated by a blue-red gradient color band, where the maximum deformation is 10 mm.

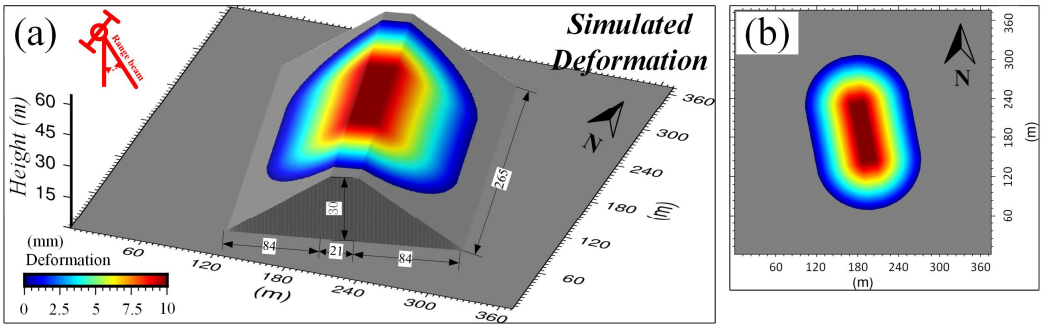

Figure 4. (**a**) The three-dimensional display of simulated dam deformation, (**b**) The front view of simulated dam deformation.

In Table 1, we present the cross angle ϕ under four specific conditions: 0°, 30°, 60°, and 90° and calculate the corresponding conversion parameter ε for three dam slopes. To better align with the influence of the incident angle in reality, we set it to 36.4° for TSX-Spotlight, 56.8° for CSK-Stripmap, and 44° for Sentinel-1 TOPS for the simulation.

Table 1. The conversion parameters in various SAR sensors on the fore- and back-slope with varied ϕ.

SAR Sensors	η (°)	ϕ (°)	ε		
			Fore-Slope (Sa)	Crest (Sc)	Back-Slope (Sb)
TSX-spotlight	36.4	0	0.90	0.80	0.52
		30	0.90	0.80	0.56
		60	0.88	0.80	0.67
		90	0.80	0.80	0.80
CSK-Stripmode	56.8	0	0.75	0.55	0.21
		30	0.73	0.55	0.26
		60	0.68	0.55	0.38
		90	0.55	0.55	0.55
Sentinel-1 TOPS	44	0	0.86	0.72	0.41
		30	0.85	0.72	0.46
		60	0.82	0.72	0.57
		90	0.72	0.72	0.72

In Table 1, it is observed that when the cross angle $\phi = 0°$, signifying the parallel alignment of the dam axis and satellite heading, the conversion parameter ε between slope S_a and slope S_b varies by 2~3 times. Conversely, when the cross angle $\phi = 90°$, all three slopes have the same local incidence angle in the LOS direction, that is $\varepsilon = \cos\eta$.

3.1. Settlement Simulation in Multi-Satellite SAR Interferometry

Corresponding to the simulated dam settlement in Figure 4, the simulated SAR interferograms for TSX-Spotlight, CSK-Strip, and Sentinel-1 TOPS are presented in Figures 5–7, respectively. Furthermore, the SAR interferograms from different sensors under specific cross angle ϕ (0°, 30°, 60°, and 90°) are also simulated to illustrate SAR distortion and deformation patterns. These variations in terms of the cross angle ϕ are presented in the subplot (a–d) in Figures 5–7. Finally, we conduct a quantitative analysis of SAR geometric distortion and phase gradient changes on the three slopes using the differential interference phases of the cross-sectional line, as shown in Figure 8.

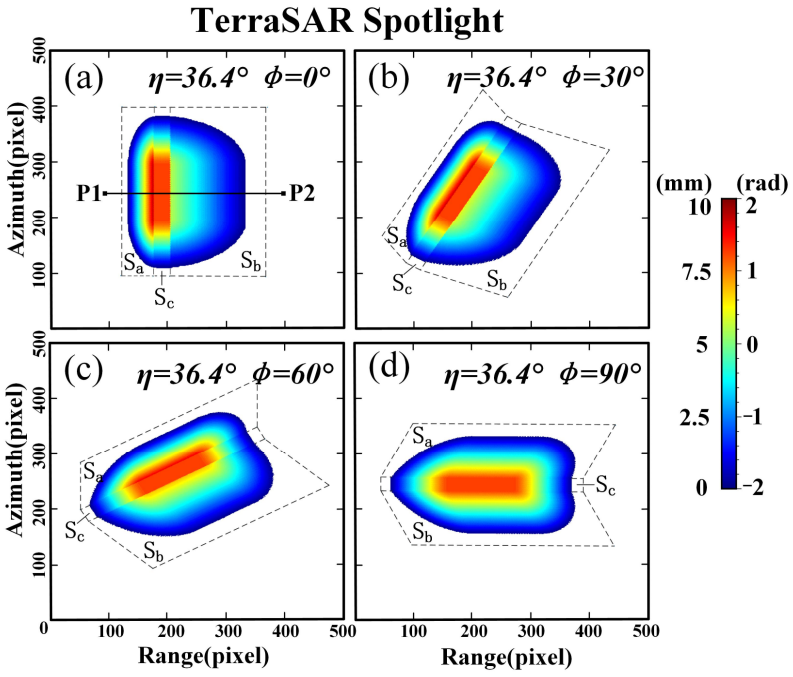

Figure 5. (**a**–**d**) are the simulated TSX differential interferograms with a cross angle ϕ of 0°,30°,60°, and 90°, and η = 36.4°.

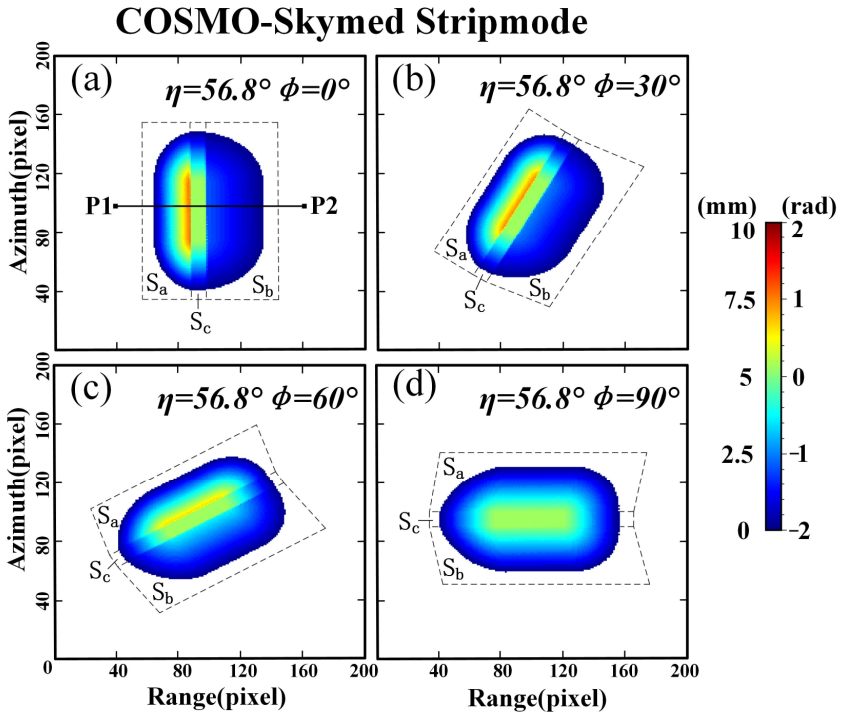

Figure 6. (**a**–**d**) are the simulated CSK differential interferograms with a ϕ of 0°,30°,60°, and 90° and η = 56.8°.

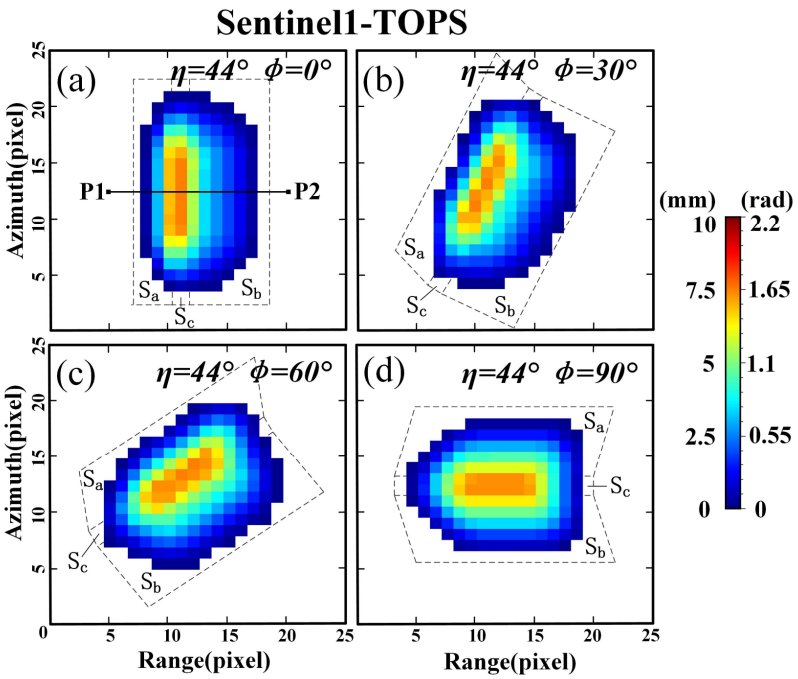

Figure 7. (**a**–**d**) are the simulated Sentinel-1 differential interferograms with a cross angle ϕ of 0°,30°,60°, and 90° and η = 44°.

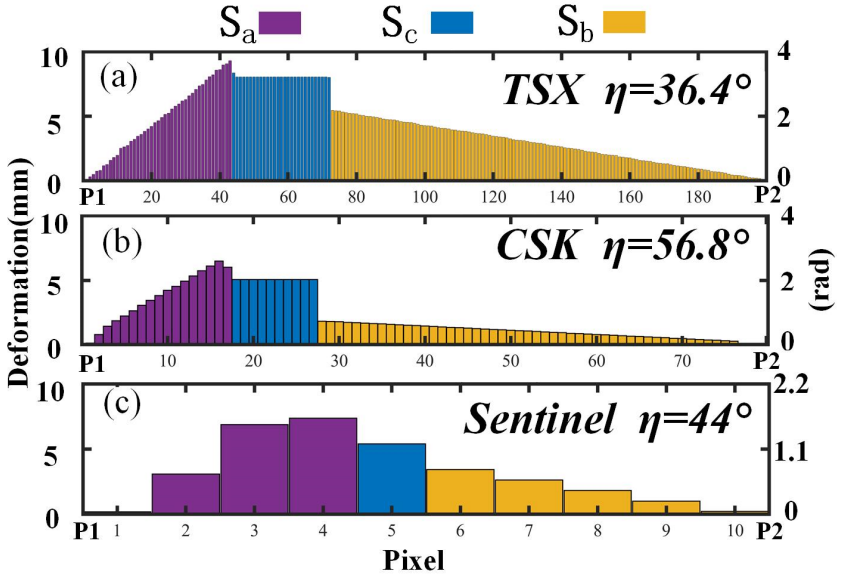

Figure 8. (**a**–**c**) are the simulated deformation and corresponding phase changes on dam cross-section P1–P2 from Figures 5a, 6a and 7a.

Figure 5 displays the simulated TSX differential interferogram with an incident angle of 36.4°. As the resolution for TSX-Spotlight is about 1 m in azimuth and range direction, we use a large size (250 × 300 pixels) in SAR geometry to show the dam's deformation in the LOS direction. With a TSX radar wavelength of 3.1 cm, 1 cm of motion on the dam slope corresponds to 4 rad phase changes. The plots in Figure 5a–d illustrate the simulated interferogram for four specific cross angles ϕ. The horizontal and vertical coordinates represent the range and azimuth pixel numbers in the SAR image coordinate system. The color bar indicates the deformation value from 0 to 1 cm, with the corresponding phase gradient ranging from −2 to 2 rad.

Figure 5a shows that in S_b the phase gradient becomes much smaller than that in S_a. The original uniform deformation pattern on the dam loses its shape and outline in SAR 2D images. Due to SAR distortion, slope S_a appears compressed higher than slope S_b.

According to Table 1, the conversion parameter ε on the dam top surface S_c remains constant. However, on slope S_a, ε reaches up to 0.9 when $\phi = 0°$ and gradually decreases as ϕ increases. When ϕ reaches 90°, the conversion parameter ε aligns with that on the top surface S_c. Meanwhile, as depicted in Figure 5, the minimum conversion parameter on slope S_c is 0.52 at $\phi = 0°$ and increases with the dam axis intersection angle ϕ.

Figure 6 illustrates the simulated differential interferogram corresponding to the simulated post-construction settlement of the dam body with a 1 cm settlement based on the CSK-strip model with an incident angle of 58.6°. The wavelength of CSK is 3.1 cm; therefore, 1 cm of deformation corresponds to 4 rad phase changes. The CSK data resolution in azimuth and range direction is about 3 m. To facilitate a visual comparison with TSX data, a magnified image with 80 × 120 pixels is employed to depict the dam in SAR geometry. The incident angle of CSK is 56.8°, resulting in pronounced SAR distortion. Although both TSX and CSK share the same radar wavelength, the phase values in Figure 6 are lower than those in Figure 5 due to the different local incidence angles on each slope.

Figure 6a shows the differential interferogram when $\phi = 0°$. Due to its larger incident angle, the proportion of the area occupied by S_a is larger than that of TSX. In addition, the difference in conversion parameter ε between the slopes becomes greater than that in TSX data, reaching 1.5 times between slope S_a and S_b and 2.6 times between slope S_b and S_c, resulting in a large phase gradient in Figure 6a–c. In Figure 6d, the conversion parameter ε is consistent across each slope, leading to smooth transitions between slopes.

Figure 7 displays a simulated differential interferogram representing the simulated dam post-contraction settlement of 1 cm, under Sentinel-1 TOPS mode. The wavelength

for S1 is 5.6 cm, meaning that 1 cm of deformation corresponds to 2.2 rad phase changes. TOPS mode data have a 5:1 resolution rate between range and azimuth direction. In order to make the dam visualization in SAR image consistent with the dam aspect ratio, a 5:1 multi-look is applied to the TOPS data. Consequently, representing the dam only takes up to about 10 × 15 pixels in SAR coordinates.

In Figure 7a, the simulated differential interferogram is presented when $\phi = 0°$. Defining the accurate intersection and boundary of S_a, S_b, and S_c is challenging in this case. The region with larger deformation is concentrated in 2~3 pixels. It could be difficult to accurately measure the 1 cm displacement on S_a surface by such limited pixels.

From the above analysis, it is evident that when the direction of the dam axis is parallel with the satellite heading, the differences in geometric distortion and the conversion parameter among the three planes of the dam are most pronounced. For analysis, we select the differential interferograms of various sensors when $\phi = 0°$ to examine the SAR geometric distortion and phase gradient change on the three slopes. Figure 8 illustrates the change in the differential interference phase of the cross-sectional line at the center of the dam. The position of the cross-sectional line is indicated in P1–P2 in Figures 5a, 6a and 7a.

In Figure 8, the x-axis represents the pixel number in the SAR image, while the y-axis on the left and right represent deformation values and phase values, respectively. The purple color in Figure 8 represents the phase in the slope S_a, blue represents the phase in the dam crest plane S_c, and yellow represents the phase in the slope S_b. The pixels of the cross-section of the dam on the three resolution SAR images exhibit significant differences. The TSX image, with a range resolution of 0.45 m, has 200 pixels in width, while the CSK image, with a range resolution of 1.18 m, has about 80 pixels in width. In the case of Sentinel-1 with a range resolution of 11.5 m (the range resolution of the original data is 2.32; since we have conducted the 5:1 multi-look, the range resolution becomes 11.5 m), there are only about 10 pixels in width.

As seen in Table 1, the conversion parameters in slopes are different. So, in Figure 8a, the phase gradients are generated at the intersection of the two surfaces in the simulated interferogram. The conversion parameter in the slope S_a is 0.9 (refer to Table 1), slightly larger than the conversion parameter 0.8 on plane S_c, leading to a 0.5 rad phase gradient between S_a and S_c. The conversion parameter for slope S_b is 0.52, resulting in a phase gradient of 1 rad between S_c and S_b. Similarly, in Figure 8b, the gradient between the S_c and S_b increases and reaches 1.2 rad, attributed to the increased local incident angle of the CSK sensor.

In general, to evaluate the true deformation of the three planes of the dam, it is necessary to carry out phase unwrapping and deformation conversion of the three planes separately by Equation (9). Extracting the deformation of the crest poses challenges due to its narrow width (approximately 8 m). Additionally, there will be a significant difference in the deformation conversion parameter as the incident angle increases on the two slopes. Thus, it is necessary to perform phase unwrapping and deformation reduction separately to ensure the reliability of the monitoring results.

3.2. Comparing the Multi-Satellite SAR Dam Slope Phase Inversion from 2D SAR Geometry to 3D Geolocation

To further analyze the recoverability of dam shrinkage deformation using various SAR sensors, geocoding was performed based on the simulated differential interferograms in the previous section. Figure 9a presents a three-dimensional schematic diagram of the simulated dam surface deformation in terms of geographic coordinates. Figure 9b–d depict the three-dimensional diagrams of the geocoded interferograms in Figure 5a, Figure 6a, and Figure 7a, respectively. (For a better visual effect, we use the azimuth and incident angles shown in Figure 4 to display the three-dimensional perspective effect).

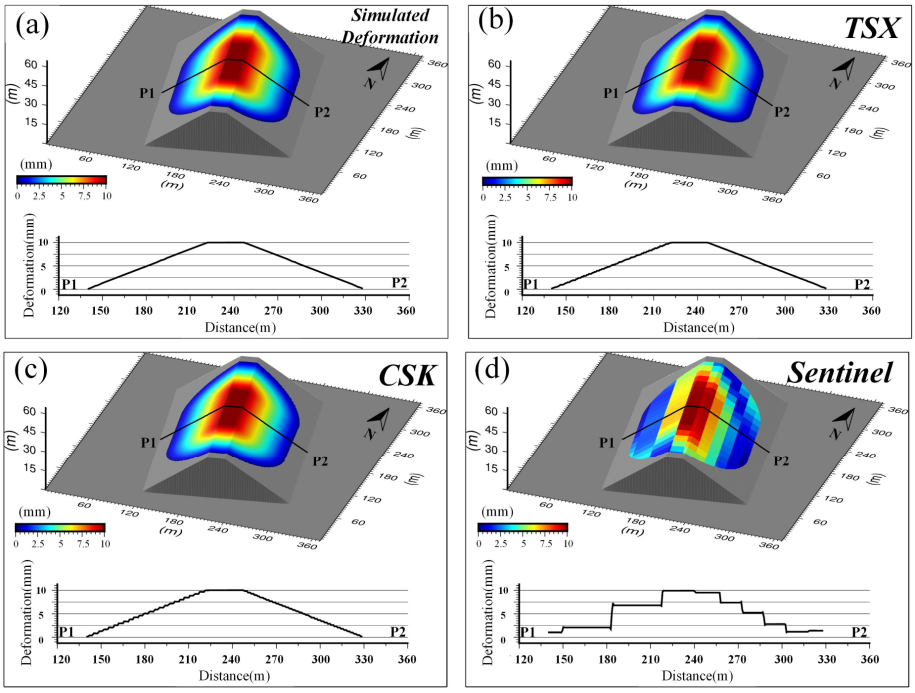

Figure 9. The deformation inversion of the simulated dam from 2D SAR geometry to 3D geolocation by multi-satellite SAR data. (**a**) is the simulated deformation. (**b**–**d**) are the 3D geolocation by TSX, CSK and Sentinel, respectively.

Referring to the central cross-section lines of the dam P1–P2, the profile line obtained by TSX is very smooth. However, the profile line derived from CSK shows obvious discontinuity, primarily caused by insufficient pixel sampling on surfaces S_a and S_b. In addition, the profile line of S_b is smoother than that of S_a, owing to more sampling, as indicated in Figure 8. In other words, slope S_b, with a higher local incidence angle in SAR image, can more effectively capture deformation details better than slope S_a.

For Sentinel-1, the pixels of S_a and S_b are limited, resulting in stepwise curves in the cross-section deformation lines. Based on the analysis above, it is evident that the small dam slope deformation monitoring by SAR sensors with different resolutions exhibits a notable scale effect. Only the high-resolution SAR image can extract the surface deformation of dam slopes in detail.

According to the analysis conducted in this study on 1 cm deformation in the differential interferogram, for post-construction settlement monitoring of a 30 m high dam slope, 3 m resolution SAR images are practically enough for deformation retrieval. However, for more detailed deformation monitoring, 1 m resolution SAR images are definitely preferred.

4. Slope Settlement Derived from Multi-Satellite SAR Interferograms

4.1. Testing Site

Gongming Reservoir (as depicted in Figure 10) was built along the surrounding hills with six adjacent earth-rock-filled dams forming a fan-shaped water area. The reservoir is designed to maintain a water level of 59.7 m, boasting a volumetric storage capacity of 142 million cubic meters and covering an expansive 6 square kilometers. All those dams were built on hilly terrain with homogeneous earth-filled structures, except for the No. 3 dam, which is a clay core earth and rock-filled dam. The total length of the dam crest is 4.3 km. The earth filling reaches heights ranging from 30 to 50 m. The maximum elevation of the dam peaks at 50.7 m.

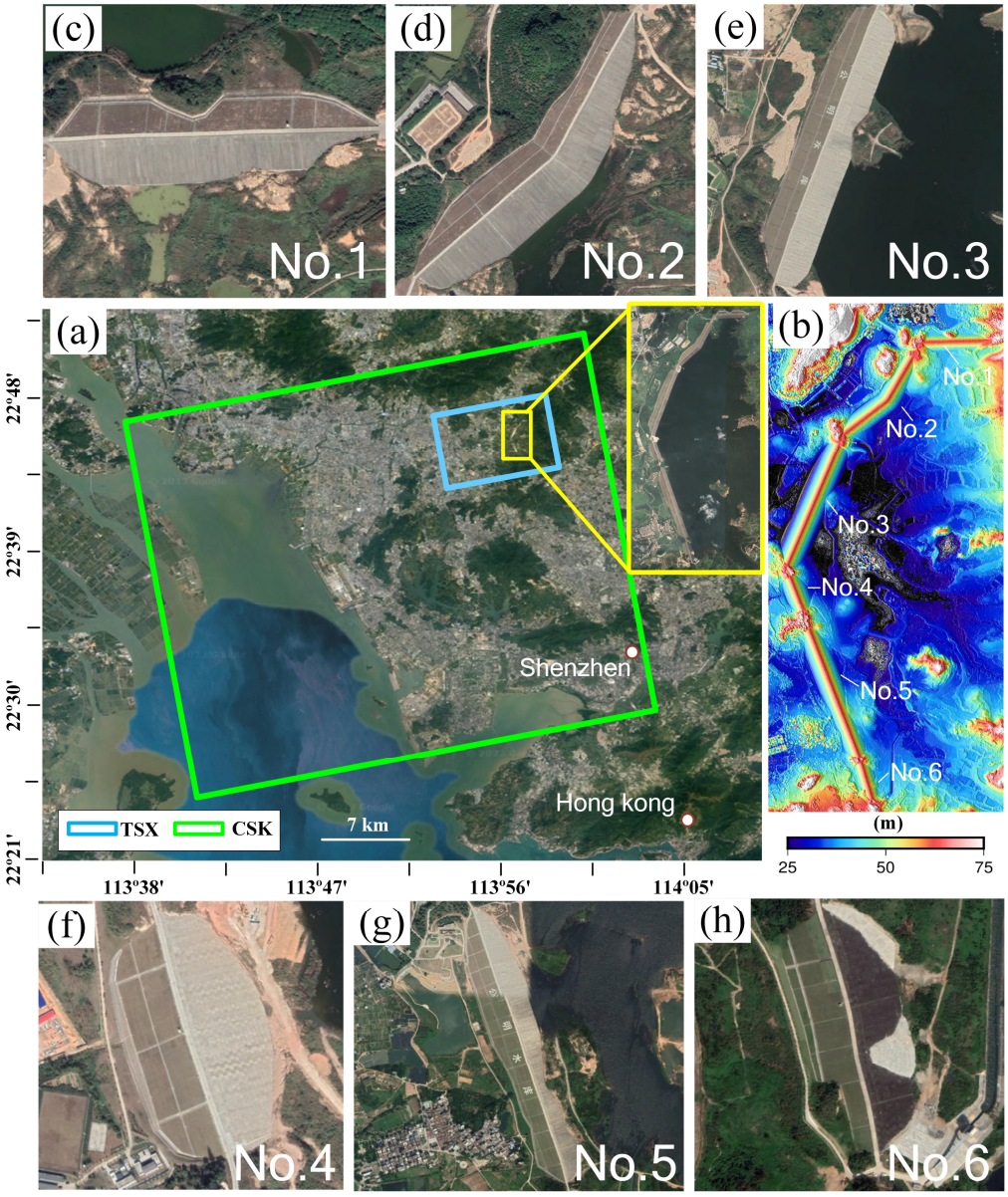

Figure 10. The geographic position and images of Gongming Reservoir. (**a**) The geographical location of Shenzhen Reservoir, TSX, and CSK image coverage. (**b**) DEM of six dams. (**c**–**h**) Optical image of No. 1–6 dams.

Gongming Reservoir's geographical location and layout are illustrated in Figure 10; Figure 10a presents an optical image, while Figure 10b displays the DEM of the six dams acquired by UAV in December 2016. The resolution of the DEM is 0.45 m and the height accuracy is approximately 20 cm. Optical images of the six dams are depicted in Figure 10c–h.

The upstream slope of each dam is constructed with a 0.3-m-thick concrete panel, while the downstream slope is covered with soil ranging from 0.3 to 0.5 m in thickness and adorned with planted grass. On the dam crest, there is a concrete road with an 8 m width (refer to Figure 11b). Additionally, a 0.7 m high waterproof wall has been constructed near the upstream slope on the crest, and a 0.3 m high protective wall is positioned on the opposite grass slope side.

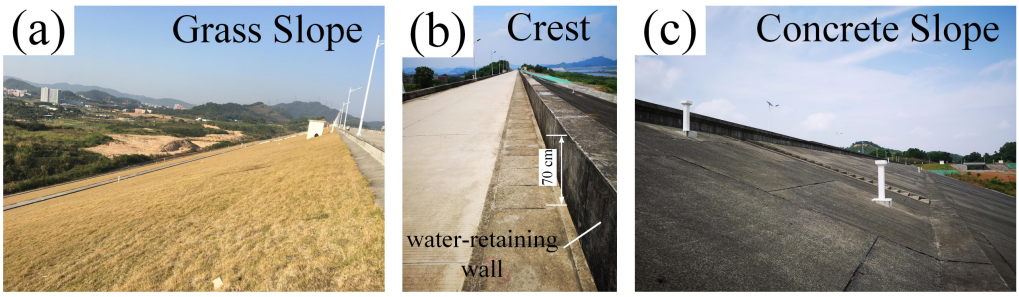

Figure 11. Images of the dam surface of the reservoir. (**a**) Image of the grass-planted slope. (**b**) Image of the crest. (**c**) Image of the concrete slope.

It took 8 years to build up all six dams of Gongming Reservoir. The construction of No. 1–2 dams started in 2010 and was completed in 2013. No. 3 dam was completed by the end of 2016. And in the end of 2017, No. 4, 5, and 6 dams were completed. Since July 2017, the reservoir started to impound. To prevent the leakage of the dam basement, concrete leakage-proof walls were built at the bottom of the dam center, and curtain grouting was carried out in the weathered rock zone. The six dams are mainly homogenous earth dams with slight structural differences. Only the No. 3 dam has a clay core for waterproofing.

The earth-filling height of the six dams ranges approximately from 30 to 50 m, and their post-construction settlement period typically spans 1 to 3 years. Based on the projected construction schedule, the primary post-construction settlement period of the No. 1 and No. 2 dams occurred from 2013 to 2014, while that of the No. 3 dam transpired from 2016 to 2018. No. 4, No. 5, and No. 6 dams experienced their main settlement periods from 2017 to 2019. As the multi-satellite SAR data used in this study have a considerable overlap in the first half of 2017, the paper focuses on studying No. 4 and No. 5 with large deformation during this period.

4.2. Dam Surface Scatterers and Coherence in Different SAR Sensors

We gathered three types of ascending SAR data of the Gongming reservoir including TSX-Spotlight (TSX-SL), COSMO-SkyMed stripmode (CSK-SM), and Sentinel-1 TOPS (S1), all acquired between March to June 2017. The detailed imaging parameters are outlined in Table 2. The range resolution of TSX-SL, CSK-SM, and S1 are 0.45 m, 1.2 m, and 2.3 m, respectively. In the processing of Sentinel-1 TOPS data, a 4:1 multi-looking was conducted to maintain a similar aspect ratio of the dam, considering the substantial difference between azimuth and range resolutions. Table 2 reveals that the temporal baselines of multi-satellite SAR data are approximately identical. According to the dam post-construction mechanism, the dam surface deformation trend during three months can be regarded as partially linear. Consequently, a time interval difference of a few days is not expected to introduce significant deformation values to the DInSAR interferograms.

Table 2. Main parameters of multi-satellite SAR data in Shenzhen Gongming reservoir.

Satellite	TSX-Spotlight	CSK-Strip Mode	Sentinel-TOPS
Orbit orientation	Ascending	Ascending	Ascending
Band	X (3.12 cm)	X (3.12 cm)	C (5.60 cm)
Polarization	VV	VV	VV
Acquisition time	27 February 2017 26 May 2017	1 March 2017 7 May 2017	12 March 2017 4 June 2017
Heading	349.2°	349.4°	347.6°
Incidence	36.4°	35.0°	44.0°
Range sampling	0.45 m	1.18 m	2.32 m
Azimuth sampling	0.86 m	2.07 m	14.0 m
Multi-look	1:1	1:1	4:1

Figure 12a–f present the SAR images of six dams obtained from ascending TSX-SL data. The scattering intensity on the concrete panel of the upstream slope appears notably weak, which is similar to the intensity of the calm water surface This phenomenon can be attributed to the specular reflection of the smooth concrete panel and its large local incident angle. Consequently, the coherence of the concrete slope is considerably low, leading to the conclusion that the reliable interference phase cannot be extracted from the concrete panels in the interferograms. In contrast, the scattering intensity of the downstream grass slope becomes pronounced when the dam axis is parallel to the SAR heading direction. Meanwhile, when the intersection angle ϕ between the dam axis and the SAR heading direction increases, the grass slope scattering intensity decreases correspondingly.

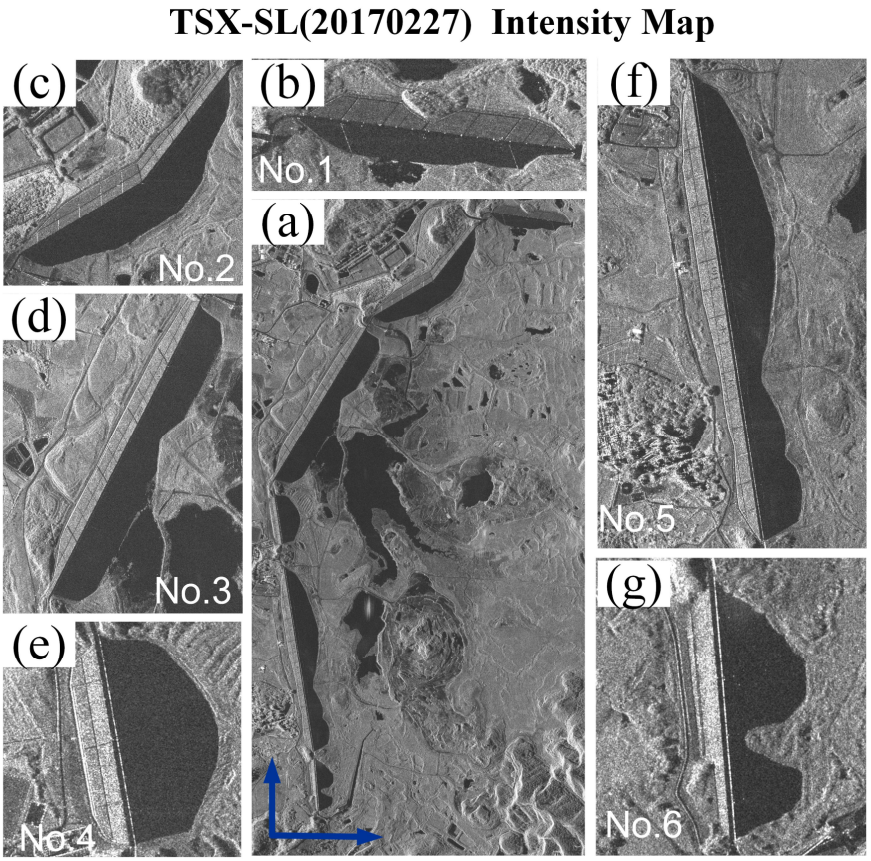

Figure 12. (**a**) SAR image of Gongming Reservoir captured in TSX data on 27 February 2017. (**b**–**g**) are the SAR image of No. 1–6 dams.

Furthermore, the waterproofing on the crest of No. 4, 5, and 6 dams exhibit a distinct and discernible linear texture in SAR images, due to dihedral angle reflection, resulting in high scattering intensity. However, for the remaining dams, the angle between the waterproofing and the satellite flight is so large that the scattering intensity is weak and difficult to identify.

The SAR image of the six dams in ascending CSK-SM data is shown in the Appendix A (Figure A1). Despite the lower resolution of CSK-SM, approximately 2.5 times less than that of TSX-SL, the radar scattering characteristics of the concrete panel and grass slope remain similar. However, for Sentinel-1 -TOP data, the dams are almost invisible (refer to Figure A2 in the Appendix A for details). A 4:1 multi-look processing has been completed for a similar aspect ratio, and the resolution of Sentinel data is around 10 m both in azimuth and in range direction. Notably, the concrete and grass slopes, spanning approximately 100 m in length, correspond to merely 7–9 pixels in the SAR image. This limitation leads to an unclear outline of these slopes in Sentinel-1 images. However, as the scattering intensity

of the grass slope is much higher than that of the concrete panel, the boundary between the grass slope and the concrete surface of the dam body can be visually distinguished.

Taking the No. 4 dam of Gongming Reservoir as an example, Figure 13 illustrates the geometric distortion characteristics of the dam in various SAR images. The TSX-SL data, with a resolution of 0.45 m, can reflect the structure of the dam well, covering approximately 250 × 300 pixels. In the CSK-SM data, with a resolution of 1.18 m, the linear features such as waterproofing on the dam crest can still be distinguished, and the dam coverage is about 80 × 110 pixels. For Sentinel-1 TOPS data with about 10 m resolution (after the 4:1 multi-look) in range direction, it is difficult to distinguish the dam body, and the dam covers about 15 × 20 pixels. The linear texture features produced by the dihedral corner reflection of the waterproofing on the crest can be observed in both the TSX and CSK data, but it is difficult to distinguish between the dam crest and the slopes in the Sentinel data. The scattering intensity of the concrete panel in the X-band and C-band Sar data is quite low, which is similar to the calm water surface.

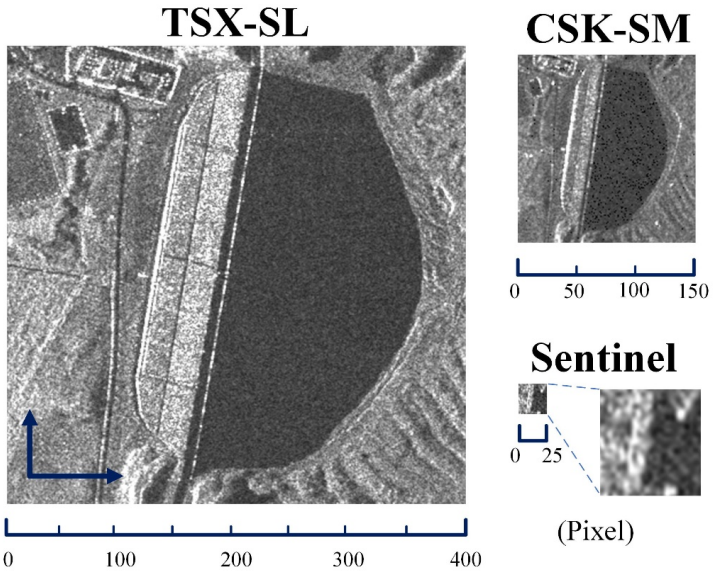

Figure 13. No. 4 dam image in multi-source SAR.

4.3. The Dams' Settlement in Multi-DInSAR Images

Figure 14 shows ascending differential interferograms of six dams in the spring of 2017 using different SAR sensors. In general, the differential interferometric phase of the grass slope is well maintained. To illustrate the resolution differences among various SAR data, the images are presented based on the pixel size in SAR coordinates. The low resolution of Sentinel data makes the original differential interferometric image nearly invisible (We enlarge it five times for better visualization). The differential interferometric phase of high-resolution TSX exhibits the best clarity with clear fringe visibility. The visibility of CSK fringes is slightly worse than that of TSX, while the S1 differential interferometric phase of the grass slope can hardly be recognized. According to the construction progress of Gongming Reservoir, the No. 1 and No. 2 dams tend to be stable and there is no post-construction settlement effect in 2017. The differential interference fringes on the surfaces of dams No. 1 and No. 2 have the same color, confirming their stability. Because of the shallow filling of the No. 6 dam, it is difficult to recognize the deformation signal from the interferometric phase. There is a slight deformation on the No. 3 dam during this time. However, there is significant deformation on the No. 4 and No. 5 dams as seen in dense fringes there.

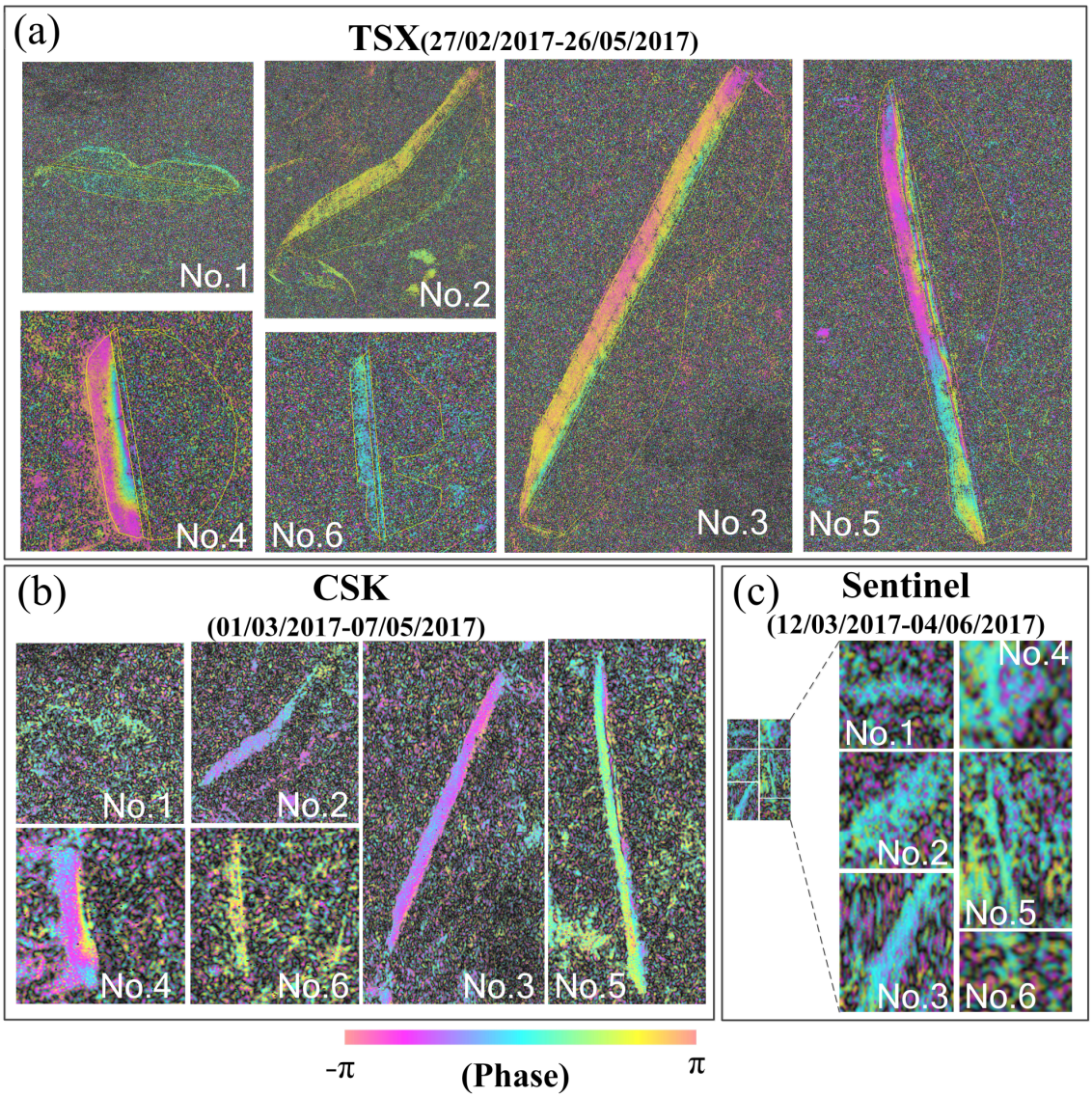

Figure 14. (**a**–**c**) are the differential interferograms of six dams by TSX, CSK and Sentinel, respectively.

Figure 15a–f illustrate the coherence map of No. 4–5 dams based on multi-satellite SAR data. The coherence map derived from the Sentinel data is enlarged five times for better visualization. In Figure 15, it is evident that the coherence for the grass slope is high. The coherence map of TSX data exhibits smoothness with consistently high values. As for CSK data, the grass slope shows high coherence except for the location near the dam crest. Although the Sentinel data shows good coherence between the two slopes of the dam, it is difficult to distinguish the difference between the grass and concrete slopes there. Especially, the top of the No. 5 dam shows obvious decorrelation, resulting in unreliable phase values in the differential interferograms. Figure 15 reveals that the waterproofing on the crest of No. 4 and 5 dams presents linear texture and good coherence in TSX-SL and CSK-SM differential interferograms (refer to the larger version of Figure 15a). However, the Sentinel-1 TOPS data cannot distinguish waterproofing and its texture characteristics due to its lower resolution.

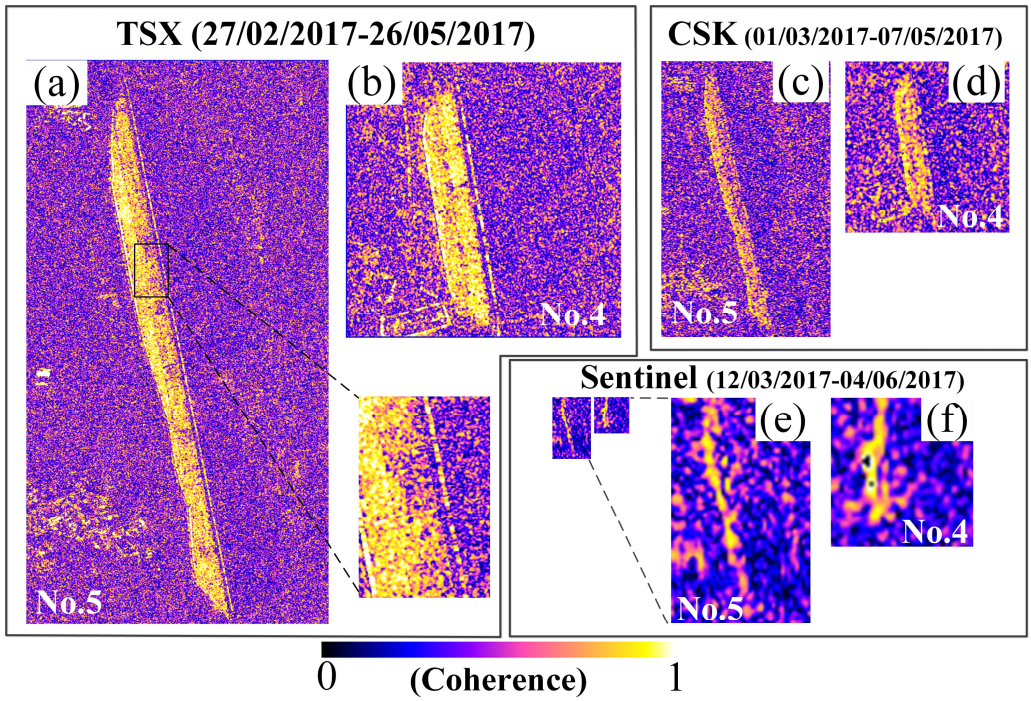

Figure 15. The coherence image by the multi-satellite SAR data. (**a**,**c**,**e**) are the coherence image of No. 5 dam by TSX, CSK and Sentinel, respectively. (**b**,**d**,**f**) are the coherence image of No. 4 dam by TSX, CSK and Sentinel, respectively.

In Figure 16, we have applied the minimum cost flow method for phase unwrapping to the differential interferograms of No. 4 and No. 5 dams from Figure 14. Pixels with coherence values below 0.6 and intensity below a specific threshold are filtered out. The initial value for phase unwrapping, located in the stable area at the bottom of the dams, was set to 0. The unwrapped interferogram of the Sentinel data is enlarged five times.

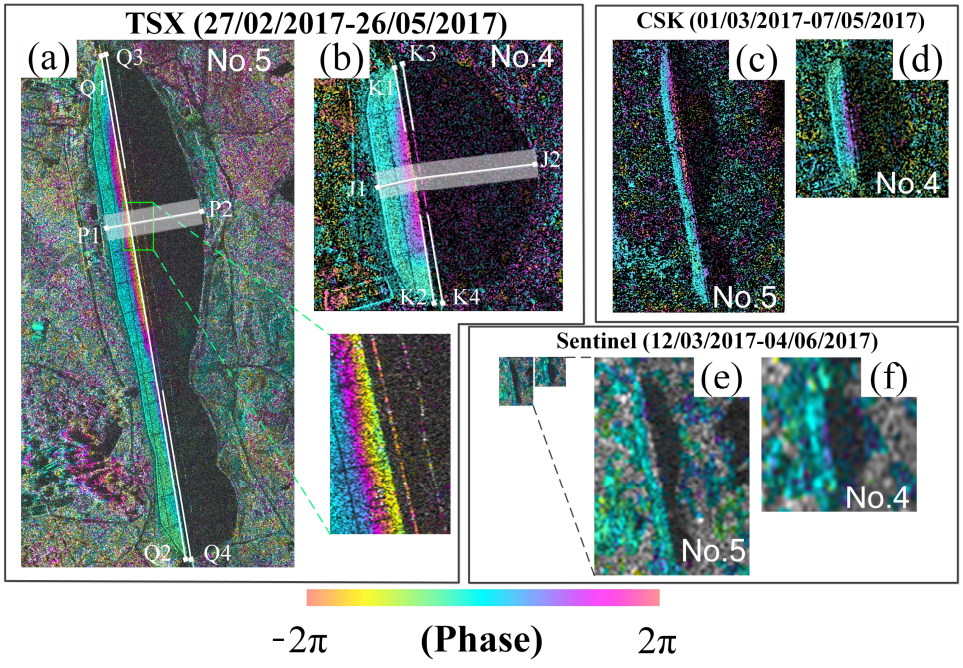

Figure 16. The unwrapped interferogram of the multi-satellite SAR image, showing in a phase period of 2π. (**a**,**c**,**e**) are the unwrapped interferogram of No. 5 dam by TSX, CSK and Sentinel, respectively. (**b**,**d**,**f**) are the unwrapped interferogram of No. 4 dam by TSX, CSK and Sentinel, respectively.

For a better visualization in Figure 16, we superimpose the unwrapped differential interferogram on the SAR intensity image. The TSX data, with its highest resolution and coherence, exhibits the most distinct deformation fringes. It is evident that the bottom of the dam remains stable, while the dam crest suffers the largest settlement. The deformation of linear features (waterproofing) at the crest of No. 4 and No. 5 dams can also be clearly observed (refer to the enlarged views in Figure 16a,b).

Figure 16c,d show the unwrapped interferograms of CSK which suffer more noise compared with TSX data due to its lower resolution, but the deformation characteristics extracted from the No. 4 and No. 5 dams are almost consistent with TSX. For the Sentinel data, the unwrapped phase at the top of the No. 5 dam is filtered out due to the low coherence. It is observed that the deformation gradient near the dam top is substantial, leading to decorrelation issues.

4.4. Dam Settlement Analysis in Different SAR Sensors

To illustrate the post-construction settlement of No. 4 and No. 5 dams in various SAR sensors, we extract deformation curves from the multi-satellite SAR interferograms. In Figure 16, for the No. 4 dam, a longitudinal section line K1–K2 at the top of the grass slope and waterproofing K3–K4 is drawn. The profile line of J1–J2 is selected at the middle of the dam where the largest deformation occurs. Similarly, for the No. 5 dam, the longitudinal profile lines are defined on the top of the grass slope Q1–Q2 and on the waterproofing on the crest Q3–Q4. Also, a profile P1–P2 is drawn in the area with the most significant deformation to further analyze the details of dam deformation.

Figure 17 illustrates the deformation curves of the longitudinal section line and the cross-section line of the area with the largest deformation on the No. 4 dam, which are extracted from the high-quality points (coherence higher than 0.6) in the unwrapped TSX, CSK, and S1 interferograms. The temporal baselines of different SAR sensors are between March and June 2017, lasting for nearly three months, with a slight mismatch (no more than 15 days). The specific time is indicated in Figure 17b,d,f. Considering the small difference in temporal baselines, the post-construction settlement characteristics of the dam based on multi-DInSAR results should be consistent. In addition, the deformation by water pressure can be ignored because the impoundment started after the SAR acquisition time.

Figure 17a,c,e presents LOS deformation results of the longitudinal section line at the top of the grass slope K1–K2 and waterproofing on the crest K3–K4, extracted from TSX, CSK, and S1 unwrapped differential interferograms, respectively. The y-axis on the left of Figure 17a,c,e represents the embankment filling height of the dam clay (in m), depicted by a purple line. The y-axis on the right represents the LOS deformation (in mm). The blue points show the LOS deformation curve extracted along the K1–K2 profile line at the top of the grass slope, and the red point shows the LOS deformation curve extracted from the K3–K4 profile line of the waterproofing on the crest. There are no valid measurement points extracted from the concrete slope, due to the low intensity and decorrelation.

Figure 17a illustrates the result of the TSX data, where high-quality points extracted from K1–K2 and K3–K4 profile lines allow a reliable assessment of the deformation. The three-month post-construction settlement of the grass slope and the waterproofing exhibits the same deformation trend on the top axis of the dam, and this trend has a good correlation with filling height. The thicker the filling, the larger the deformation. It should be noted that the deformation curve of the K1–K2 section line at the top of the grass slope is separated, to a certain extent, from the K3–K4 section line deformation curve of the waterproof in the deeply filled area. This phenomenon is associated with the deformation conversion parameter ε (refer to Equation (8)) proposed in Section 2.2.

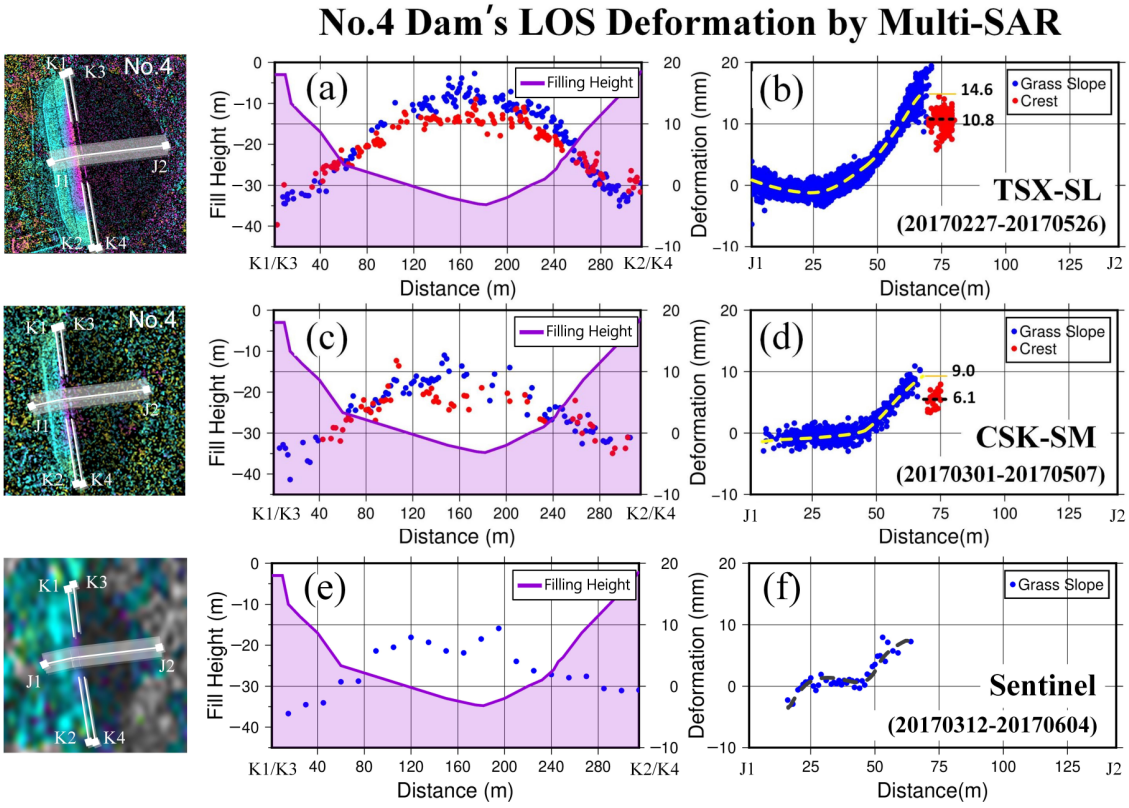

Figure 17. The deformation curves of the longitudinal section line and the cross-section line of the area with the largest deformation on the No. 4 dam, derived from multi-satellite SAR unwrapped interferograms. (**a**,**c**,**e**) show LOS deformation results of the longitudinal section line of the top of the grass slope K1–K2 (red points) and of waterproofing on the crest K3–K4 (blue points), extracted from TSX, CSK, and S1 data, respectively. (**b**,**d**,**f**) show the deformation curves of the J1–J2 cross-section lines in the middle of the No. 4 dam extracted from TSX, CSK, and S1 data, respectively. The purple line represents embankment filling height.

Figure 17c presents the result of CSK data; with the number of points on the K1–K2 and K3–K4 profile lines being nearly half of that in TSX, which is expected due to the difference in resolution of the two types of data. The CSK result exhibits some volatility due to its greater phase noise. In general, the two-month deformation trend of the grass slope and the waterproofing manifested in the CSK data is highly consistent with the three-month deformation trend of TSX, indicating that deformation in the area with deeper filling is higher.

Figure 17e illustrates the results of the K1–K2 profile line of the grass slope of the Sentinel data. Only 21 sparse points are obtained from the profile line, due to the low resolution. Meanwhile, the phase of the K3–K4 profile line of waterproofing could not be extracted. The deformation trend of the grass slope in the Sentinel data is still correlated with the depth of the dam body filling, and it is consistent with the trends in TSX and CSK. The amount of deformation in the middle area of the dam body has accumulated to about 9 mm in 3 months.

Figure 17b,d,f present the deformation curves of the J1–J2 cross-section lines in the middle of the No. 4 dam, obtained from the unwrapped interferograms of TSX, CSK, and Sentinel. To minimize the influence of phase noise in individual points and obtain more samples, we set the width of the J1–J2 cross profile line to 40 m, which is indicated by the white bands along J1–J2 in Figure 17b. The blue point represents the LOS deformation of the grass slope, the averaged value is denoted by the yellow dashed line. The averaged value of the grass slope near the crest is marked with black points. The red point indicates

the LOS deformation of the waterproof on the crest. The black dashed line represents the fitting averaged value of the red points and is marked with text.

Figure 17b depicts the results obtained from the TSX data. The post-construction settlement of the No. 4 dam at the lower part of the grass slope is minimal within three months. The post-construction deformation of the dam body gradually increases from the middle of the grass slope, reaching a maximum of 15 mm (equal to 2π phase cycle) at the top area of the grass slope within three months. However, the deformation of the waterproofing on the crest is approximately 11 mm, which is 3.8 mm less than that of the grass slope.

Figure 17d displays the deformation results of the CSK data along the cross-section line. Similar to the TSX results, the post-construction settlement of the dam on the bottom of the grass slope exhibits a small amount of deformation within two months. Starting from the middle of the grass slope, the deformation of the dam body gradually increases and reaches 10 mm at the top of the grass slope, while that of the waterproofing is about 6 mm. This indicates a 4 mm gradient between them. Referring to Equation (9), due to the different local incident angles of two planes, the LOS deformation of the dam crest and the top of the grass slope exhibits variations in both TSX and CSK data. It is necessary to correct the deformation with reference to the local incident angles of different satellites on different dam planes.

Figure 17f illustrates the results obtained from the Sentinel data, revealing a maximum deformation of approximately 9 mm along the cross-sectional line. It can be vaguely distinguished that there is no settlement deformation in the lower part of the grass slope while the deformation in the middle and upper parts gradually increases. The Sentinel results exhibit partial agreement with TSX and CSK, indicating that the low resolution of Sentinel-1 can capture dam deformation under suitable incident angles, baselines, and slope angles. However, compared to the deformation captured by TSX within three months, the deformation captured by Sentinel appears somehow underestimated. Moreover, due to the low resolution of Sentinel, it is hard to distinguish the specific location of the waterproofing on the crest and extract its deformation phase.

Figure 18 presents the deformation curves of the longitudinal section and the cross-section of the area with the largest deformation on the No. 5 dam, obtained from the high-quality points in multi-satellite SAR unwrapped interferograms. Figure 18a,c,e depict LOS deformation results of the longitudinal section of the top of the grass slope Q1–Q2 and waterproofing on the crest Q3–Q4, extracted from TSX, CSK, and Sentinel, respectively. Figure 18b,d,f illustrate the deformation curves of the P1–P2 cross-section lines in the middle of the No. 5 dam extracted from TSX, CSK, and Sentinel, respectively. The x-axis and y-axis settings, as well as the temporal baseline for SAR sensors, remain consistent with those in Figure 17.

In Figure 18b,d,f, the deformation curves of the P1–P2 cross-section lines in the middle of the No. 5 dam are displayed, extracted from the unwrapped interferograms of TSX, CSK, and Sentinel. The x-axis and y-axis settings, along with the color-coded points, maintain consistency with those in Figure 17b. The width of the cross-section line is set at 50 m.

Regarding the TSX result presented in Figure 18b, the deformation along the profile line of the grass slope is consistently depicted, indicating favorable phase quality for TSX. The settlement observed at the top of the grass slope measures approximately 20 mm (equivalent to 2.6π phase cycles). Notably, there exists a noticeable gradient difference of approximately 6.2 mm between the yellow dashed line, representing the averaged deformation at the top of the grass slope, and the black dashed line, signifying the averaged deformation at the crest.

In Figure 18d, the cross-sectional deformation of the No. 5 dam obtained by CSK is presented. The deformation trend of the grass slope and the crest are consistent with TSX. Considering that the temporal baseline of CSK is less than TSX for about one month, the maximum deformation by CSK is reduced proportionally. Nonetheless, a deformation disparity of around 6.6 mm still exists between the top of the grass slope and the crest.

Figure 18f illustrates the deformation curve of the cross-section of the No. 5 dam obtained by the Sentinel data. This result significantly differs from the TSX and CSK findings. Notably, in Figure 18f, the phase noise at the bottom of the grass slope is prominent, and points in the middle and upper sections of the grass slope are masked due to coherence loss due to large deformation. Furthermore, the low resolution of the Sentinel data hinders the extraction of deformation information at the waterproofing on the crest.

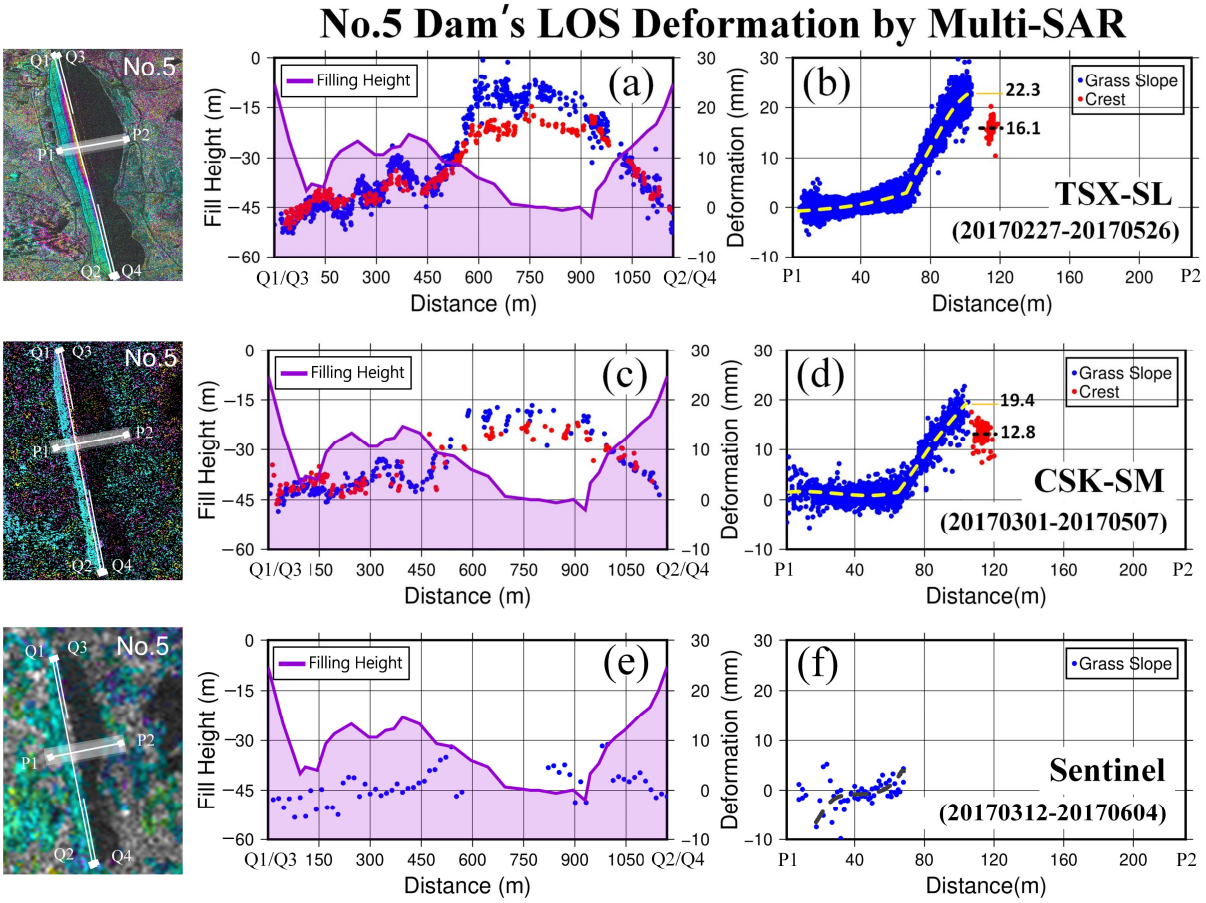

Figure 18. The deformation curves of the longitudinal section line and the cross-section line of the area with the largest deformation on the No. 5 dam, derived from multi-satellite SAR unwrapped interferograms. (**a**,**c**,**e**) show LOS deformation results of the longitudinal section line of the top of the grass slope Q1–Q2 (red points) and of waterproofing on the crest Q3–Q4 (blue points), extracted from TSX, CSK, and S1 data, respectively. (**b**,**d**,**f**) show the deformation curves of the P1–P2 cross-section lines in the middle of the No. 5 dam extracted from TSX, CSK, and S1 data, respectively. The purple line represents embankment filling height.

The LOS deformation results for the No. 4 and No. 5 dams highlight a noticeable correlation between post-construction settlement and earth-filling height within the first year after construction. Approaching the top of the dam, the deformation becomes greater. The result also reveals the difference between the deformation curve of the top of the grass slope and that of the waterproofing on the crest. With reference to the previous simulation and derivations, the difference could be attributed to the conversion parameter ε. Therefore, utilizing Equation (9) and considering the deformation difference between the grass slope and crest from Figures 17b,d and 18b,d, it is possible to perform an inverse calculation to determine the actual conversion parameter ε. This derived value can then be validated against the theoretical one.

The theoretical conversion parameter ε of slopes can be calculated by Equation (8), according to the dam slope angle and orientation from DEM. Figure 19 presents the

theoretical conversion parameter values of the six dam slopes. The conversion parameter values are labeled through a blue-red color bar from 0.5 to 1.0. Since the incident angles of the TSX and CSK data only differ by 1.4° in this case, the deformation conversion parameters of the two data are similar. Therefore, only the TSX results are displayed.

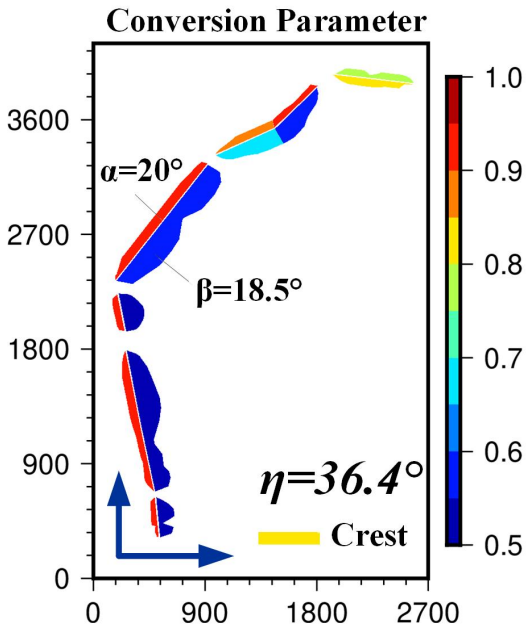

Figure 19. The theoretical conversion parameters of six dams of Gongming Reservoir in TSX data.

In Figure 19, all the grass slopes for the dams have a slope angle of 20°, while the concrete slopes have a consistent slope angle of 18.5°. Considering that most grass slopes directly face the SAR LOS direction, the conversion parameter for the grass slope is about 0.9. However, as most concrete slopes deviate from the radar LOS direction, the conversion parameters for these slopes are mainly less than 0.6. Specifically, for the No. 1 dam, its axis direction is nearly perpendicular to the flight direction of the satellite, resulting in ϕ being close to 90°. The local incident angles and the conversion parameters of the grass slope and the concrete slope are almost identical. Regarding the No. 2 dam, the zigzag design of the dam results in four slopes with different orientations, each corresponding to a distinct conversion parameter. For the crest of all dams, the deformation conversion parameter remains constant regardless of dam orientation and is consistently 0.8.

Similar to the simulated dam deformation in Section 3, we assume that the deformation on the top of the grass slope and the crest are consistent. Subsequently, the converted deformation of the crest is considered the truly vertical deformation of the top of the grass slope, and the practical conversion parameter ε_p of the grass slope can be calculated by the observed LOS deformation and converted vertical deformation on the top of the grass slope. Table 3 shows the results of the theoretical and practical conversion parameters ε of the No. 4 and No. 5 dams. It also indicates the consistency between the theoretical and practical values, which is calculated by $\frac{\varepsilon_t - |\varepsilon_t - \varepsilon_p|}{\varepsilon_p} * 100\%$. The theoretical deformation conversion parameters for the No. 4 and No. 5 dams are the same due to their identical slope angle and orientation. The conformity of the theoretical and practical conversion parameters ε_p are higher than 80% for both the TSX and CSK data. The conformity of the CSK data is slightly higher than that of the TSX data in both dams, suggesting that the real dam post-construction settlement phenomenon may not be as ideal as estimated and simulated, and the discrepancy does show some highlights for us.

Table 3. The theoretical and practical conversion parameters ε of No. 4 and No. 5 dams' slopes.

SAR Sensor	Dam	ε		Difference	Conformity
		Theoretical	Practical		
TSX-SL	No. 4	0.90	1.08	0.18	80%
	No. 5	0.90	1.11	0.21	77%
CSK-SM	No. 4	0.90	0.81	−0.09	90%
	No. 5	0.90	0.83	−0.07	92%

5. Conclusions

In this paper, we propose a conversion parameter to derive the dam slope deformation from SAR geometry and investigate the monitoring capabilities of both C-band and X-band SAR sensors for monitoring post-construction settlement of earth-rock dams. Through simulations based on this model, we analyze in detail how local incidence angle and dam heading angle influence line-of-sight (LOS) deformation conversion. The validity of the model is confirmed through the utilization of actual SAR data for verification.

The outcomes of the simulation results indicate that the dams with their axis being parallel to the SAR heading direction, exhibit the most significant disparity in converting parameters between fore-slope and back-slope. The greatest impact appears on the dam top, where we find obvious discontinuity of the deformation curves and fringes. In contrast, when the dam axis is perpendicular to the SAR heading direction, the deformation conversion parameters remain consistent across all slopes.

The practical experiment conducted at Shenzhen Gongming Reservoir highlights the superior performance of high-resolution TSX and CSK SAR. In contrast, Sentinel-1 TOPS data falls short in fully capturing the dam slope deformation, primarily due to both its low-resolution and phase decorrelation. Despite simulated Sentinel-1 results suggesting the possibility of extracting vertical deformation from limited pixels, the actual data contradicts this assumption. This implies that the decorrelation is a more critical factor than resolution. The high-resolution D-InSAR proves to be a valuable tool for accurately evaluating the consolidation process of newly constructed earth dams, serving the precise needs of pumped storage hydroelectric power stations.

Author Contributions: Conceptualization, Tao Li; Methodology, Jie Liu; Software, Sijie Ma; Formal analysis, Sijie Ma and Qiang Shan; Investigation, Jie Liu and Qiang Shan; Writing—review and editing, Jie Liu, Tao Li and Weiping Jiang; Supervision, Tao Li; Funding acquisition, Tao Li. All authors have read and agreed to the published version of the manuscript.

Funding: This research is supported by the National Natural Science Foundation of China (NSFC), grant number 42074031, 41674032, and the National Key R&D Program of China: 2018YFC1503603.

Data Availability Statement: The datasets presented in this article are not readily available because the data are part of an ongoing study. Requests to access the datasets should be directed to the corresponding author.

Acknowledgments: The authors thank the German Aerospace Agency (DLR) for providing the TerraSAR-X Spotlight data sets under proposal motagh_GEO1916. We thank Mahdi Motagh very much for the SAR data and the suggestion to the paper. Thanks to Jiping Li from Vastitude technology company who provides the COSMO-SkyMed datasets. We also thank Shenzhen Water-related high technology development company for creating the dam high-resolution DEM and the field investigation.

Conflicts of Interest: The authors declare no conflict of interest.

Appendix A

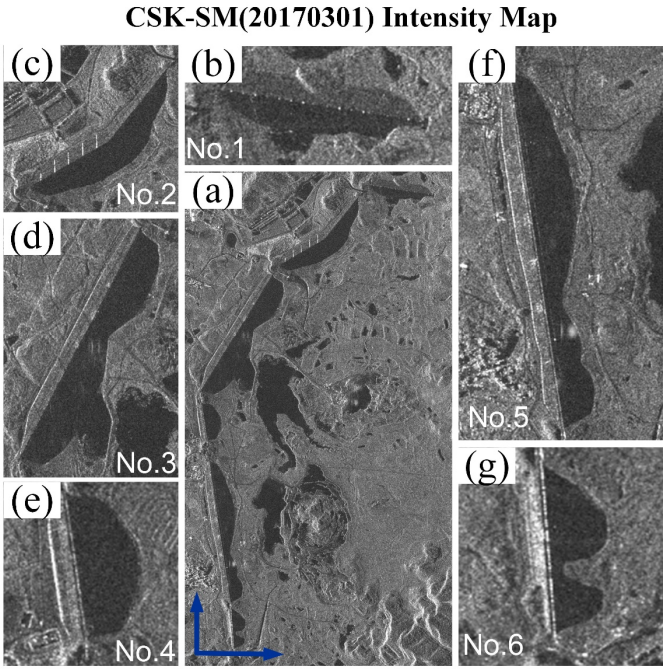

Figure A1. (**a**) The SAR image of Gongming reservoir by CSK sensor. (**b**–**g**) are the SAR image of No. 1–6 dams.

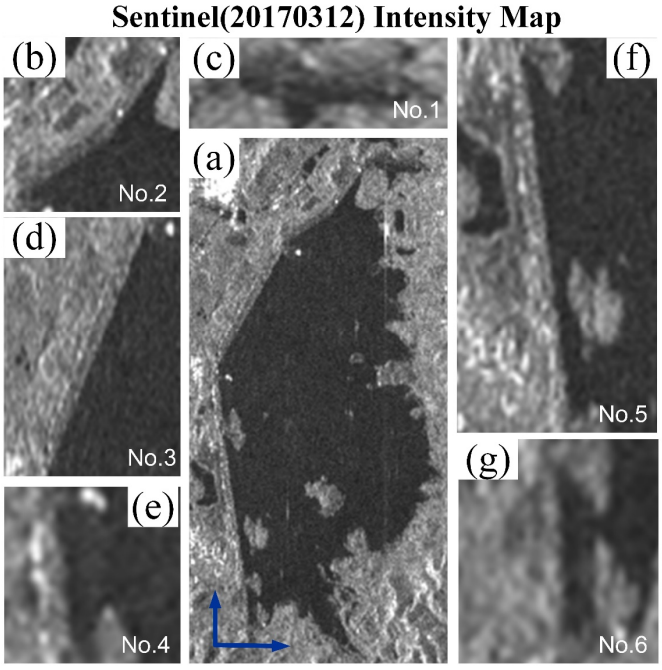

Figure A2. (**a**) The SAR image of Gongming reservoir by Sentinel sensor. (**b**–**g**) are the SAR image of No. 1–6 dams.

References

1. Ministry of Water Resources, People's Republic of China. *2019 Statistic Bulletin on China Water Activities*; China Water & Power Press: Beijing, China, 2019.
2. Du, Z.; Ge, L.; Ng, A.H.M.; Zhu, Q.; Horgan, F.G.; Zhang, Q. Risk assessment for tailings dams in Brumadinho of Brazil using InSAR time series approach. *Sci. Total Environ.* **2020**, *717*, 137125. [CrossRef] [PubMed]

3. Neokosmidis, S.; Elias, P.; Parcharidis, I.; Briole, P. Deformation estimation of an earth dam and its relation with local earthquakes, by exploiting multitemporal synthetic aperture radar interferometry: Mornos dam case (central greece). *J. Appl. Remote Sens.* **2016**, *10*, 026010. [CrossRef]
4. Milillo, P.; Burgmann, R.; Lundgren, P.; Salzer, J.; Perissin, D.; Fielding, E.; Biondi, B.; Milillo, G. Space geodetic monitoring of engineered structures: The ongoing destabilization of the Mosul dam, Iraq. *Sci. Rep.* **2016**, *6*, 37408. [CrossRef] [PubMed]
5. Emadali, L.; Motagh, M.; Haghshenas Haghighi, M. Characterizing post-construction settlement of the Masjed-Soleyman embankment dam, Southwest Iran, using TerraSAR-X SpotLight radar imagery. *Eng. Struct.* **2017**, *143*, 261–273. [CrossRef]
6. Wang, T.; Perissin, D.; Rocca, F.; Liao, M.-S. Three Gorges Dam stability monitoring with time-series InSAR image analysis. *Sci. China Earth Sci.* **2010**, *54*, 720–732. [CrossRef]
7. Al-Husseinawi, Y.; Li, Z.; Clarke, P.; Edwards, S. Evaluation of the Stability of the Darbandikhan Dam after the 12 November 2017 Mw 7.3 Sarpol-e Zahab (Iran–Iraq Border) Earthquake. *Remote Sens.* **2018**, *10*, 1426. [CrossRef]
8. Tomás, R.; Cano, M.; García-Barba, J.; Vicente, F.; Herrera, G.; Lopez-Sanchez, J.M.; Mallorquí, J.J. Monitoring an earthfill dam using differential SAR interferometry: La Pedrera dam, Alicante, Spain. *Eng. Geol.* **2013**, *157*, 21–32. [CrossRef]
9. Selvakumaran, S.; Rossi, C.; Marinoni, A.; Webb, G.; Middleton, C. Combined insar and terrestrial structural monitoring of bridges. *IEEE Trans. Geosci. Remote Sens.* **2020**, *58*, 7141–7153. [CrossRef]
10. Qin, X.; Ding, X.; Liao, M.; Zhang, L.; Wang, C. A bridge-tailored multi-temporal dinsar approach for remote exploration of deformation characteristics and mechanisms of complexly structured bridges. *ISPRS J. Photogramm. Remote Sens.* **2019**, *156*, 27–50. [CrossRef]
11. Grenerczy, G.; Wegmüller, U. Deformation analysis of a burst red mud reservoir using combined descending and ascending pass ENVISAT ASAR data. *Nat. Hazards* **2012**, *65*, 2205–2214. [CrossRef]
12. Di Martire, D.; Iglesias, R.; Monells, D.; Centolanza, G.; Sica, S.; Ramondini, M.; Calcaterra, D. Comparison between Differential SAR interferometry and ground measurements data in the displacement monitoring of the earth-dam of Conza della Campania (Italy). *Remote Sens. Environ.* **2014**, *148*, 58–69. [CrossRef]
13. Zhou, W.; Li, S.; Zhou, Z.; Chang, X. Remote Sensing of Deformation of a High Concrete-Faced Rockfill Dam Using InSAR: A Study of the Shuibuya Dam, China. *Remote Sens.* **2016**, *8*, 255. [CrossRef]
14. Zhou, W.; Li, S.; Zhou, Z.; Chang, X. InSAR Observation and Numerical Modeling of the Earth-Dam Displacement of Shuibuya Dam (China). *Remote Sens.* **2016**, *8*, 877. [CrossRef]
15. Ullo, S.L.; Addabbo, P.; Di Martire, D.; Sica, S.; Fiscante, N.; Cicala, L.; Angelino, C.V. Application of DInSAR Technique to High Coherence Sentinel-1 Images for Dam Monitoring and Result Validation through In Situ Measurements. *IEEE J. Sel. Top. Appl. Earth Obs. Remote Sens.* **2019**, *12*, 875–890. [CrossRef]
16. Li, T.; Motagh, M.; Wang, M.; Zhang, W.; Gong, C.; Xiong, X.; Liu, J. Earth and Rock-Filled Dam Monitoring by High-Resolution X-Band Interferometry: Gongming Dam Case Study. *Remote Sens.* **2019**, *11*, 246. [CrossRef]
17. Zhao, C.; Lu, Z.; Zhang, Q.; de la Fuente, J. Large-area landslide detection and monitoring with ALOS/PALSAR imagery data over northern california and southern oregon, USA. *Remote Sens. Environ.* **2012**, *124*, 348–359. [CrossRef]
18. Bonforte, A.; Guglielmino, F.; Coltelli, M.; Ferretti, A.; Puglisi, G. Structural assessment of Mount Etna volcano from Permanent Scatterers analysis, Geochem. *Geophys. Geosyst.* **2011**, *12*, Q02002. [CrossRef]
19. Eriksen, H.Ø.; Lauknes, T.R.; Larsen, Y.; Corner, G.D.; Bergh, S.G.; Dehls, J.; Kierulf, H.P. Visualizing and interpreting surface displacement patterns on unstable slopes using multi-geometry satellite SAR interferometry (2D InSAR). *Remote Sens. Environ.* **2017**, *191*, 297–312. [CrossRef]
20. Guan, Z. *Hydraulic Structural Design Volume Six: Earth and Rock Filled Dam*, 2nd ed.; China Water & Power Press: Beijing, China, 2014. (In Chinese)